Spring 1-1-2013

Numerical Analysis of Synthetic Jet Flow Control on a Vertical Tail

Jeffrey Louis Martin
University of Colorado at Boulder, jeffmrtn12@gmail.com

Numerical Analysis of Synthetic Jet Flow Control on a
Vertical Tail

by

Jeff Martin

B.S., Rensselaer Polytechnic Institute, 2010

A thesis submitted to the

Faculty of the Graduate School of the

University of Colorado in partial fulfillment

of the requirements for the degree of

Master of Science

Department of Aerospace Engineering Sciences

2013

This thesis entitled:
Numerical Analysis of Synthetic Jet Flow Control on a Vertical Tail
written by Jeff Martin
has been approved for the Department of Aerospace Engineering Sciences

_____

Kenneth Jansen

_____

Michael Amitay

_____

Michel Rasquin

Date _____

The final copy of this thesis has been examined by the signatories, and we find that both the
content and the form meet acceptable presentation standards of scholarly work in the above
mentioned discipline.

Martin, Jeff (Aerospace Engineering)

Numerical Analysis of Synthetic Jet Flow Control on a Vertical Tail

Thesis directed by Prof. Kenneth Jansen

Airflow over a stabilizer-rudder assembly is simulated on an unstructured grid using a streamline upwind Petrov-Galerkin (SUPG) weighted residual finite element formulation of the incompressible Navier-Stokes equations. These studies seek to determine the effectiveness of synthetic jet flow control in increasing side force over the vertical tail. The two models under investigation are the Beta model, with 12 jets aligned along the span of the stabilizer, and a Beta model scaled up by a factor of 1.969, with 24 jets aligned along the span of the stabilizer. These two models have Reynolds numbers of 3.6×10^5 and 7.1×10^5, respectively, where both are based on the mean aerodynamic chord. The flow solver, Phasta, is used to run these simulations. URANS simulations on the Beta model with a $5°$ sideslip angle and $20°$ rudder deflection angle show that unsteady blowing with a blowing ratio of 1.0 increases the total side force coefficient by 14% with respect to the baseline. The C_p data obtained as a function of percent chord showed improvement in C_p from unsteady blowing in the outboard region, but negligible change in the inboard region. This data is in agreement with experimental values. Speed isosurface data was obtained for the Beta model with a $0°$ sideslip angle and $30°$ rudder deflection angle, with steady blowing. It was found that these isosurfaces create ridges and valleys along the span, suggesting interference between the jets. The same result was found for the scaled-up Beta model with a $0°$ sideslip angle and $30°$ rudder deflection angle, with steady blowing.

Dedication

I dedicate this thesis to my parents, Scott and Carolyn, and my brother, Matthew, who encouraged me to pursue graduate school and have given me support over the years.

Acknowledgements

I want to give a special thanks to my advisor, Dr. Kenneth Jansen, for his support and expertise. I'd also like to thank my research colleagues, Dr. Michel Rasquin, Kedar Chitale, and Ben Matthews. It has truly been a pleasure doing research with this group; I have gained a lot of valuable insight from working with all of you.

Contents

Tables

Table

Figures

Figure

Chapter 1

Introduction

Aerodynamic control surfaces have an operating regime that is strongly influenced by the degree to which the airflow stays attached to the surface. When flow separation becomes massive, it limits all aerodynamic control surfaces, including the rudder, to a certain range of deflection angles. The purpose of the rudder is to change the effective shape of the vertical tail, which increases the side force. At large rudder deflection angles, the boundary layer separates from the surface, and there is a drastic loss of streamwise momentum. When this occurs, the side force is reduced, which makes aircraft yaw motions more difficult to achieve and may lead to a loss of stability. However, flow control offers an opportunity to counter these adverse effects, allowing enhanced performance at higher rudder deflection angles.

Synthetic jets are a form of active flow control, where the jets have zero net mass flux and rely on the free-stream velocity, or cross flow, for the supply of fluid. This unique feature allows them to transfer linear momentum to the flow system without any net mass injection (see Glezer and Amitay [3]). They are formed by imposing a time-alternating velocity field, which is achieved by the motion of a piezoelectrically driven diaphragm [3]. The vibration of the diaphragm results in a series of suction-blowing phases, where upstream and spanwise fluid is pulled into the jet and then ejected downstream. The interaction between the jets and the cross flow over the airfoil surface create the *Coandă* effect, where the added momentum will displace the local streamlines and thereby keep the flow attached longer. This approach requires the operating frequency to be much larger than the characteristic flow frequency (e.g. shedding frequency of the airfoil). This way, the

interaction domain between the jets and the cross flow is independent of the global timescale of the flow, and aerodynamic forces are invariant with the actuation frequency [3]. A reduced frequency $(F^+) > 10$ times that of the characteristic flow frequency has been shown to be effective in this regard [1].

The following chapters will present the methodology used to obtain the numerical results, followed by a discussion of the results. A short mathematical description of the flow solver will be given, as well as a discussion of the mesh and boundary conditions used. A presentation of the results obtained will follow. The final chapter will give concluding remarks and describe future work to be performed on this project.

Chapter 2

Flow Solver Formulation

The governing equations of motion in this problem are the Navier-Stokes equations, a system of nonlinear partial differential equations which express momentum conservation. Due to their inherent nonlinearity, there is no closed-form solution to these equations, making numerical methods the only practical way to to solve them for a desired domain and set of boundary conditions. The equations can however be simplified by treating the fluid as incompressible. This assumption is valid if the Mach number is less than ~ 0.3, which is the case for the problem of interest. The strong form of the incompressible Navier-Stokes equations will be discussed, followed by a description of the finite element method used to discretize the weak form.

2.1   Strong form

The strong form of the incompressible continuity and momentum equations (see Gresho [4]) can be written as

$$u_{i,i} = 0 \tag{2.1}$$

$$u_{i,t} + u_j u_{i,j} = -p_{,i} + \tau_{ij,j} + f_i \tag{2.2}$$

where the pressure and body force terms are implicitly divided by the density ρ. τ_{ij} is the deviatoric stress tensor given by

$$\tau_{ij} = \nu(u_{i,j} + u_{j,i}) \tag{2.3}$$

where ν is the kinematic viscosity μ/ρ.

2.2   Weak form - finite element discretization

The finite element weak form of the Navier-Stokes equations (2.2) makes use of discrete weight and solution function spaces, defined on some spatial domain $\Omega \cup \Gamma$, in N dimensions. The boundary is broken into portions with natural boundary conditions, Γ_h, and essential boundary conditions, Γ_g, where $\Gamma = \Gamma_g \cup \Gamma_h$. The domain, Ω, is decomposed into n_{el} finite elements, $\bar{\Omega}_e$. The $H^1(\Omega)$ weight functions q and w_i are introduced, where $H^1(\Omega)$ represents the usual Sobolev space of functions with square-integrable values and derivatives on Ω (see Hughes [5]). Upon integrating by parts and multiplying by the weight functions, the strong form of equations (2.2) is transformed into the semi-discrete Galerkin formulation given by:

$$
\begin{aligned}
B_G(w_i, q; u_i, p) =& \int_\Omega \{w_i(u_{i,t} + u_j u_{i,j} - f_i) + w_{i,j}(-p\delta_{ij} + \tau_{ij}) - q_{,i} u_i\} \, \mathrm{d}\Omega \\
&+ \int_{\Gamma_h} \{w_i(p\delta_{in} - \tau_{in}) + q u_n\} \, \mathrm{d}\Gamma_h
\end{aligned}
\tag{2.4}
$$

Solutions for **u** and p are found when: $B_G(w_i, q; u_i, p) = 0$

However, the Galerkin method is unstable for equal-order interpolations, so additional stabilization terms are added. This yields:

$$
\begin{aligned}
B(w_i, q; u_i, p) =& B_G(w_i, q; u_i, p) + \sum_{e=1}^{n_{el}} \int_{\bar{\Omega}_e} \{\tau_M(u_j w_{i,j} - q_{,i})\mathscr{L}_i + \tau_C w_{i,i} u_{j,j}\} \, \mathrm{d}\bar{\Omega}_e \\
&+ \sum_{e=1}^{n_{el}} \int_{\bar{\Omega}_e} \{w_i \overset{\Delta}{u}_j u_{i,j} + \bar{\tau} \overset{\Delta}{u}_j w_{i,j} \overset{\Delta}{u}_k u_{i,k}\} \, \mathrm{d}\bar{\Omega}_e
\end{aligned}
\tag{2.5}
$$

where $\mathscr{L}_i$ represents the ith momentum equation

$$
\mathscr{L}_i = u_{i,t} + u_j u_{i,j} + p_{,i} - \tau_{ij,j} - f_i
\tag{2.6}
$$

The first integral of equation (2.5) is the streamline upwind/Petrov-Galerkin (SUPG) stabilization, commonly used for the incompressible formulation (see Franca and Frey [2]). The first part of the second integral was introduced by Taylor *et al.* [9] to account for the loss of momentum conservation introduced as a consequence of the momentum residual appearance in the continuity equation. The

second part of this integral is included to stabilize this new advective term. A solution is obtained when $\mathbf{u}$ and p have been found, such that:

$$B(w_i, q; u_i, p) = 0 \tag{2.7}$$

The infinite dimensional spaces are replaced by finite element spaces by writing equation (2.5) as products of weights and residuals as:

$$\sum_{i=1}^{3} \sum_{A=1}^{n_n} w_i{}^A \overset{m}{R_i}{}^A + \sum_{A=1}^{n_n} q^A \overset{c}{R}{}^A = 0 \tag{2.8}$$

which is equivalent to

$$\overset{m}{R_i}{}^A = 0 \;\forall\; i, A \tag{2.9}$$

$$\overset{c}{R}{}^A = 0 \;\forall\; A \tag{2.10}$$

where $\overset{m}{R}$ and $\overset{c}{R}$ represent the portions of the residual from the momentum and continuity equations, respectively. Both are comprised of the solution variables, interpolated by three-dimensional shape functions over each element. The present problem uses only first-order polynomials [10]; they are integrated over each element using Gaussian quadrature. The resulting system of ODEs from (2.9) and (2.10) is transformed into a non-linear system of algebraic equations, and then linearized using Newton's method to obtain

$$\begin{pmatrix} \mathbf{K} & \mathbf{G} \\ -\mathbf{G}^T & \mathbf{C} \end{pmatrix} \begin{pmatrix} \Delta \mathbf{u}_{,t}{}^{n+1} \\ \Delta \mathbf{p}_{,t}{}^{n+1} \end{pmatrix} = - \begin{pmatrix} \overset{m}{\mathbf{R}} \\ \overset{c}{\mathbf{R}} \end{pmatrix} \tag{2.11}$$

where

$$\mathbf{K} \approx \frac{\partial \overset{m}{\mathbf{R}}}{\partial \mathbf{u}}, \qquad \mathbf{G} \approx \frac{\partial \overset{m}{\mathbf{R}}}{\partial \mathbf{p}}, \qquad \mathbf{C} \approx \frac{\partial \overset{c}{\mathbf{R}}}{\partial \mathbf{p}} \tag{2.12}$$

$\mathbf{K}$, $\mathbf{G}$, and $\mathbf{C}$ are approximations to the full tangent matrices. The integration in time is accomplished with a second-order implicit predictor-corrector algorithm called the generalized-α method (see Jansen *et al.* [6]). Equations (2.11) are solved on each corrector pass at each time step with the GMRES linear algebra solver of Shakib [7].

Chapter 3

Simulation Setup

The two models under investigation are low Reynolds number representations of a full-scale flight setup. The advantage to using these smaller models is a lower overhead in terms of computational resources and experimental facilities. They allow the user to test different geometry and jet configurations much more quickly and with less expense than there would otherwise be by running with a full-scale model. Furthermore, the results obtained from these preliminary simulations provide useful insight into ways the geometric setup can be optimized for future simulations.

The geometric models were constructed to both approximate the experimental setup, and minimize the error incurred from the flow solver. The conflict encountered between these two objectives was minimal, and small enough not to compromise the integrity of the simulations.

3.1   Model Scaling Parameters

The Beta model contains 4 jet modules, each containing 3 jets for a total of 12. The model contains a stabilizer-rudder assembly mounted on a platform called the "fence", which is all enclosed within wind tunnel walls. The airfoil section is classified as a NACA 0012 with a taper ratio of 0.36 and quarter-chord sweep angle of 41.6°. The stabilizer-rudder gap is untaped, meaning flow can leak into and around the gap. The second model under investigation is a scaled-up Beta model; its stabilizer-rudder assembly is the same as that of the Beta model, but it has been scaled up by a factor of 1.969. The model contains 6 jet modules, each containing 4 jets for a total of 24. The jets, however, have not been scaled up; they are the same size as those of the Beta model. Other

geometric changes include a larger fence platform, and a smaller gap between the bottom of the rudder and the fence. Table 3.1 summarizes the main features of both models:

Parameter	Beta	Beta-scaled
c_{root}, m	0.370	0.728
c_{tip}, m	0.133	0.262
Taper ratio (λ)	0.36	0.36
MAC ($\bar{c}$), m	0.271	0.534
Span (b), m	0.533	1.05
S_{ref}, m^2	0.134	0.52
Aspect ratio (AR)	2.13	2.13
$\Lambda_{c/4}$, deg	41.6	41.6
Λ_{LE}, deg	45	45
δe_{jet}, mm	26.7	26.7
δe_{module}, mm	44.5	47.0

Table 3.1: Model scaling parameters
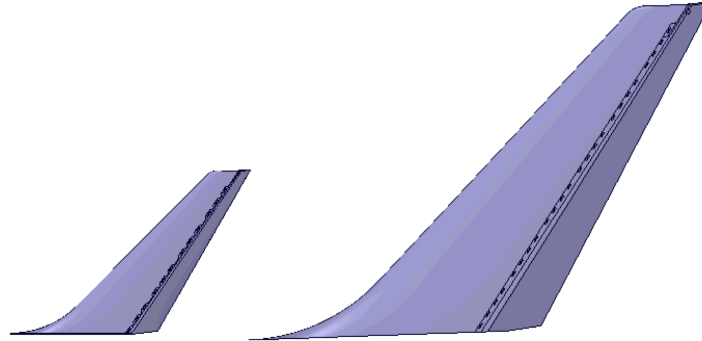
Figure 3.1: Beta and Beta-scaled
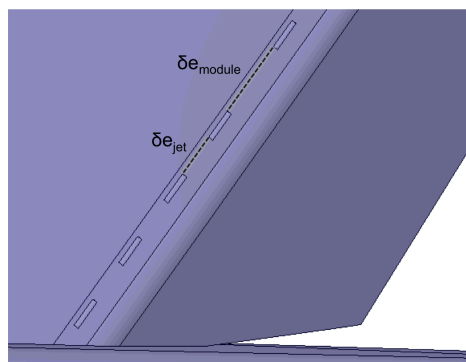
Figure 3.2: Spanwise jet spacing

The jets are grouped into modules, and all modules lie just upstream the trailing edge of the stabilizer. Two different jet configurations were tested. The full jets have a circular resonating chamber. The chamber connects to a rectangular orifice (the throat), which directs the jet flow to the free stream. The orifice has a height of 1 mm and a span of 19.1 mm. The orifice is curved, as to allow the bottom to join smoothly with the stabilizer surface. This also has the effect of forcing the jet flow to exit parallel to the free stream, adding momentum to the low-momentum region near the rudder wall. An alternative jet configuration was also tested, where the full jets were cut at a specified distance along the orifice, creating a rectangular blowing face with a height of 1 mm and a span of 19.1 mm.

The Beta model is placed in a wind tunnel test section with inlet and outlet dimensions of 0.8 x 0.8 m and a tunnel length of 5 m. The test section used for the Beta-scaled model has inlet and outlet dimensions of 1.83 x 2.44 m (width x height) and a tunnel length of 7.49 m. Lastly, two different combinations of sideslip (β) and rudder deflection (δ) angles were investigated: $\beta = 5°$, $\delta = 20°$, and $\beta = 0°$, $\delta = 30°$. Sideslip angle is measured with respect to the free stream direction (red arrow in figure 3.3, and rudder deflection angle is the angle between the chord line of the stabilizer (blue) and the chord line of the rudder (green). The two lines meet at the hinge.

Figure 3.3: β and δ
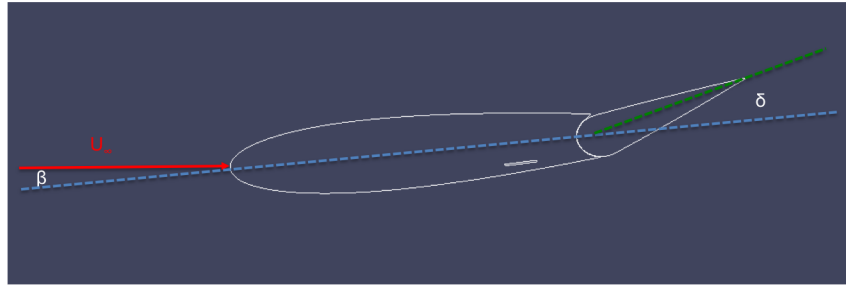
3.2   Boundary Conditions

The CAD models are converted into manifold parasolid models. The computational domain includes the faces of the wind tunnel walls and stabilizer-rudder assembly, and the empty space in between, which is treated as a fluid. The natural and essential boundary conditions are prescribed on model faces, whereas the initial conditions are prescribed on the whole computational domain. Table 3.2 lists the boundary conditions on different surfaces.

Surface	BC's
Inflow	$\mathbf{u} = (20,\ 0,\ 0)$ m/s
Outflow	pressure = 0 Pa
Slip tunnel walls	normal velocity = 0 m/s
No-slip surfaces	$\mathbf{u} = (0,\ 0,\ 0)$ m/s
Diaphragm-full jet	Parabolic velocity profile
Diaphragm-cut jet	Trapezoidal velocity profile

Table 3.2: Boundary conditions

The inlet velocity was set at 20 m/s. This corresponds to Reynolds numbers of 3.6×10^5 and 7.1×10^5 for the Beta and Beta-scaled models, respectively, where both are based on the mean aerodynamic chord. The pressure at the outflow is set to 0 Pa, which is a reference pressure since the flow is treated as incompressible. No-slip conditions are applied on all surfaces, except the tunnel walls which are modeled as slip surfaces. The initial conditions specify a velocity of $(1 \times 10^{-8},\ 0,\ 0)$ m/s and a pressure of 0 Pa. The velocity profile on the blowing face of each jet is set to match the

experimentally observed diaphragm deflection shape, and the intended blowing ratio, C_b, where

$$C_b = \frac{U_j}{U_\infty} \tag{3.1}$$

$$U_j = \frac{1}{T} \int_0^{T/2} u_j \, dt \tag{3.2}$$

and u_j is the jet velocity at the center of the jet exit without cross-flow (i.e. $U_\infty = 0$). In this context, U_j is the time-averaged jet velocity at the center of the jet exit during the outstroke phase. The integration is over only a half a cycle because a full period includes both the instroke and outstroke phases, which cancel each other. For unsteady blowing, these conditions are met by imposing a time-varying maximum velocity on the blowing face, u_{max}, given by

$$u_{max} = V_{max} \sin 2\pi f(t + \Delta t) \tag{3.3}$$

where V_{max} is the velocity amplitude, f is the jet frequency, and Δt is the time step size. For steady blowing, there is no jet frequency, so u_{max} is simply taken as a constant.

3.3   Mesh Characteristics

Discretization of the computational domain is achieved by creating a mesh of finite elements, where each has a characteristic set of nodes which contain a solution field. Building a correct mesh is of critical importance, although it is not necessarily straightforward due to the compromise between accuracy and computational resources. Using a finer mesh will reduce the discretization error, but will be more computationally demanding. As such, a coarser mesh was used in the far-field regions, and a finer mesh in the physically critical regions of the domain. The critical regions include regions near highly curved model surfaces, such as the stabilizer and rudder surfaces, and the synthetic jet paths. Two main element shapes are used in the mesh: tetrahedra and wedges, where a wedge can be divided into 3 tetrahedra. The initial mesh is mainly composed of wedges, but is converted to an all-tetrahedron mesh before doing computation with Phasta. The advantage of using an all-tetrahedron mesh over a mixed-topology mesh is that it improves the load balance

between processors. Figure 3.4 shows the Beta model surrounded by the wind tunnel walls, which defines the whole computational domain. Figure 3.5(a) shows the mesh surrounding the stabilizer nose. This region is highly refined due to the stagnation point, and high velocity gradients in this region. The no-slip condition induces high velocity gradients near the walls, and the boundary layer elements are used to capture these steep gradients. These elements are stacked up from the wall in layers of increasing thickness, as shown in figure 3.5(b).
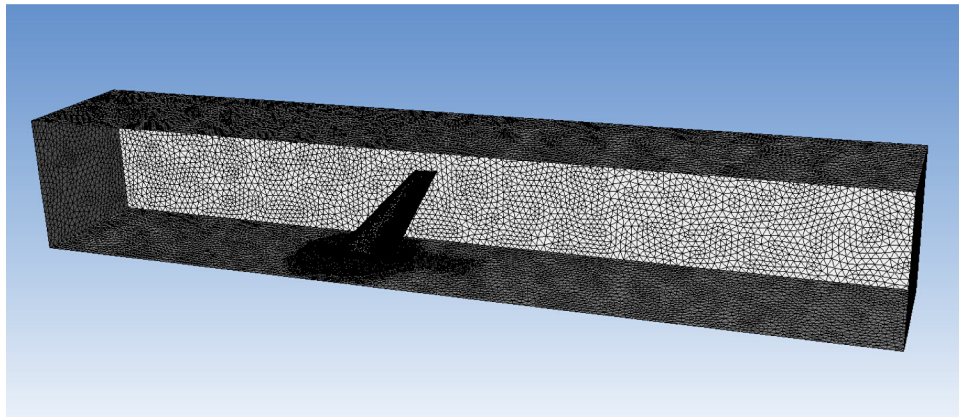
Figure 3.4: Computational domain
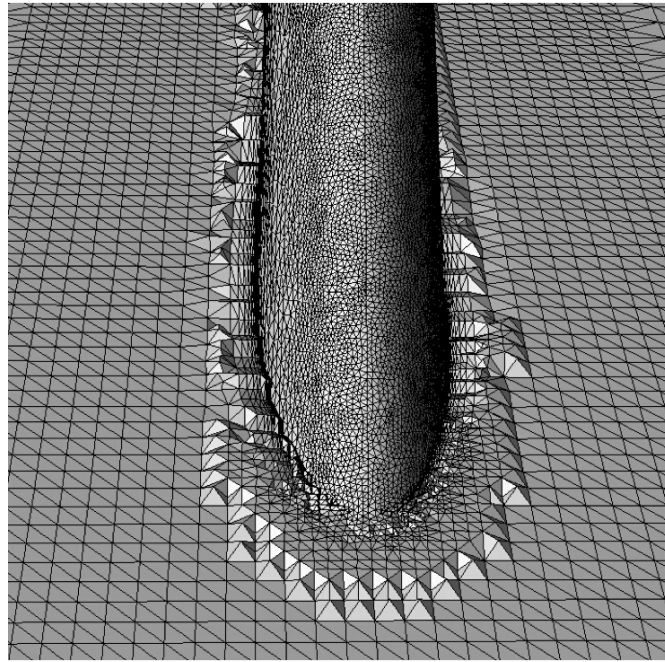
(a) Nose
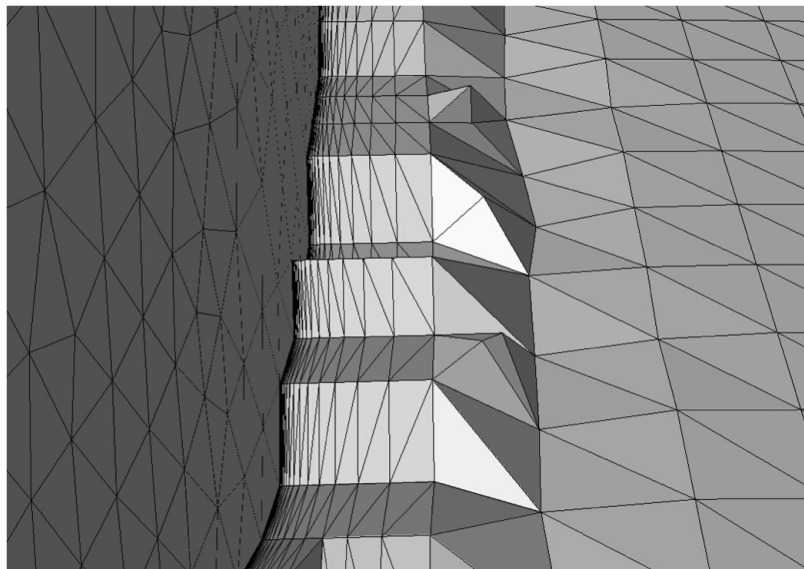
(b) Boundary layer elements

Figure 3.5: Stabilizer mesh

Particular regions of the domain, which are not necessarily associated with a particular face, can be refined by creating refinement boxes. These are defined by an origin and 3 vectors, but the vectors need not be orthogonal. This allows more flexibility in terms of isolating very specific regions that

need more refinement than their surroundings. Figure 3.6 shows a global view of the refinement regions, where a slice, parallel to the free-stream, has been taken through the mesh. There is a high level of refinement near the model, and it gradually coarsens downstream. Downstream refinement is required due to the vortices shed into the rudder wake. Moreover, the region immediately down-stream the rudder is given an especially high level of refinement in order to resolve the separated flow regime. This is apparent from figure 3.7.
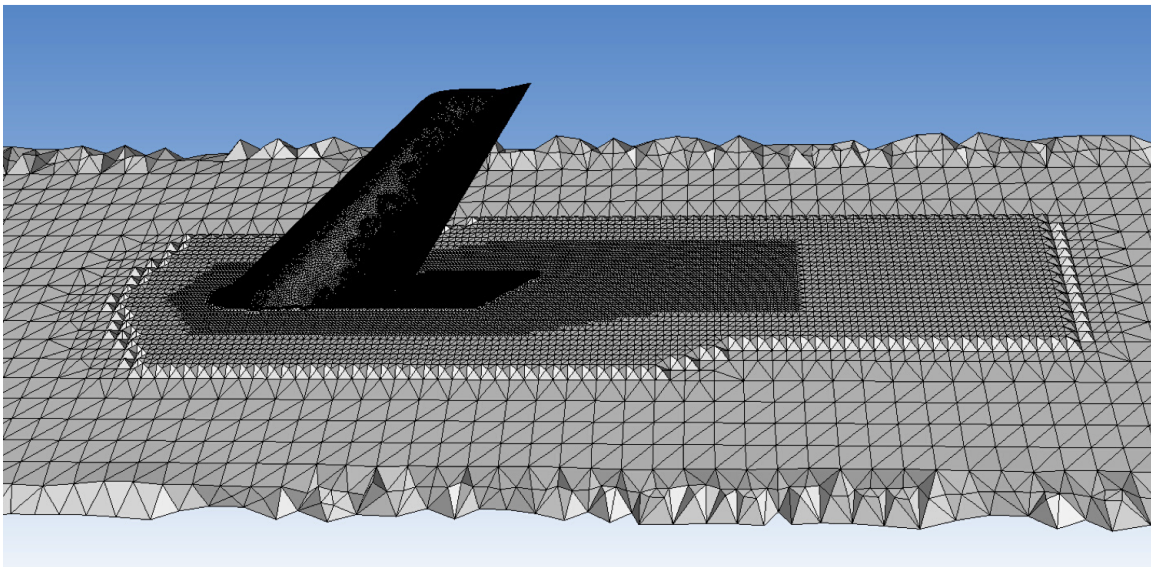
Figure 3.6: Refinement regions
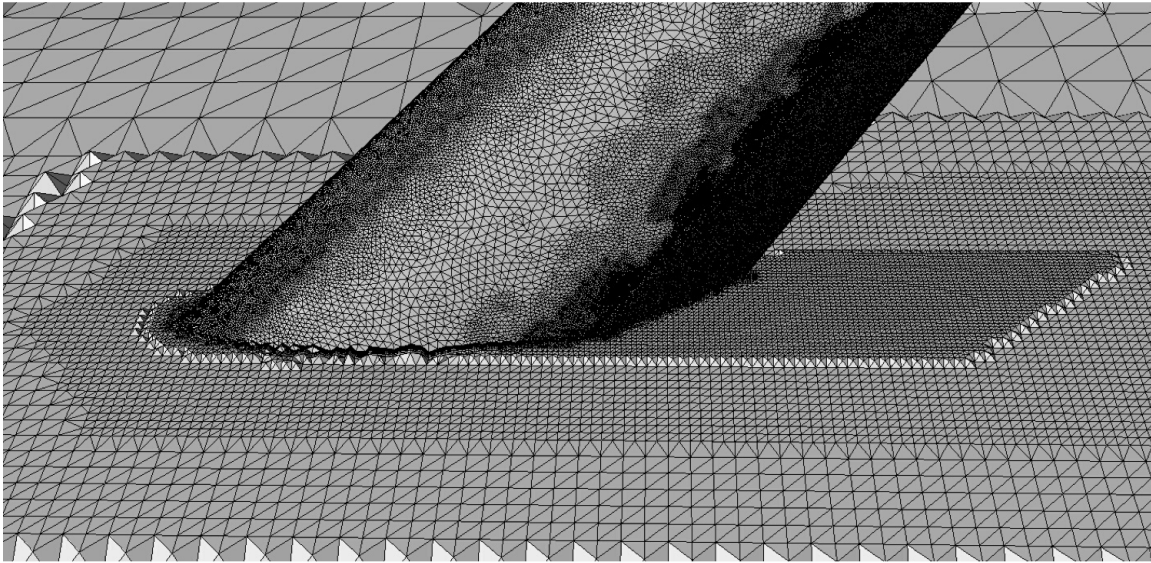
Figure 3.7: Rudder and wake refinement

The mesh surrounding a full jet from the Beta model is shown in figure 3.8(a). The jet exit fillet, shown in figure 3.8(b), is an important feature of the jets, and requires a thin boundary layer and fine mesh.
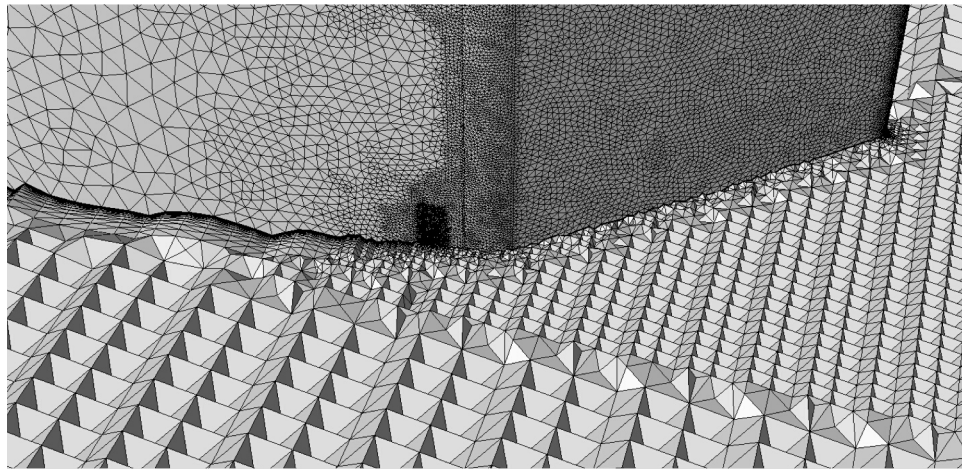
(a) Outer
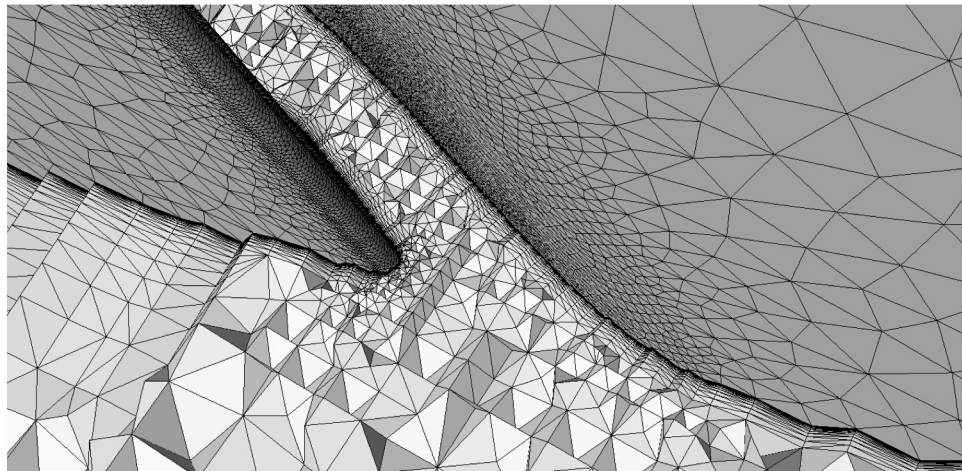
(b) Inner

Figure 3.8: Jet mesh - exterior

The jet throat mesh is fairly coarse near the inlet but becomes finer inside the throat. The high level of refinement in the throat is needed to resolve the recirculation regions that develop due to the curved surfaces. There are also small, unsteady structures that develop in the throat, which also require a very fine mesh.

Chapter 4

Simulation Results

This section covers the URANS (unsteady Reynolds-averaged Navier-Stokes) simulation results obtained for different model parameters. The turbulence model used was the Spalart-Allmaras model [8]. This is a one-equation model for the eddy viscosity. The results from both β-δ combinations will be addressed, where the two different jet configurations were tested with the Beta model, and only the cut jets were tested with the Beta-scaled model. The effectiveness of the jets is considered from multiple viewpoints; changes in pressure coefficient, speed isosurface, and side force coefficient data with respect to the baseline will be discussed. Comparisons will be made between numerical data obtained at CU Boulder and experimental data at Rensselaer Polytechnic Institute.

4.1   Beta Model - β=5°, δ=20°

The actuation frequency used in these simulations was 1600 Hz. The baseline simulation was compared with a simulation where all 12 full jets were activated in locked phase, at 180 time steps per cycle. This corresponds to a time step size of 3.472×10^{-6} seconds, or, 2° per time step. A value of V_{max} was chosen such that the parabolic velocity profile produced a value of $C_b = 1.0$. The CFD C_y for the forced case was found to be 14% higher than that for the baseline, where C_y is the side force normalized by (dynamic pressure $\times$ S_{ref}). The baseline CFD value of C_y is slightly higher than that reported by experiment, however, the forced CFD C_y differed by less than 1% with respect to the experimental value. The baseline C_y discrepancy is likely due to the limitations

of the URANS model in predicting massively separated flows. Table 4.1 shows the breakdown of C_y from different surfaces; as expected, the stabilizer and rudder contribute all of the side force.

Surface	C_y	% of total C_y
Stabilizer + rudder	0.9422	100
Stabilizer	0.7541	80.04
Rudder	0.1881	19.96
Jet paths + diaphragm	0	0

Table 4.1: C_y breakdown

The instantaneous C_y contribution from each surface is shown in figure 4.1. These plots are consistent with figure 4.1.
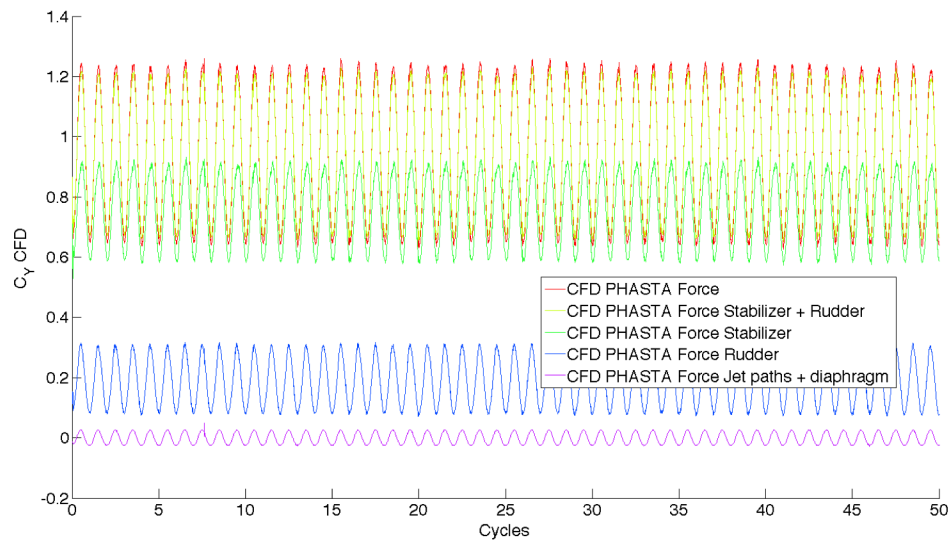
Figure 4.1: C_y - instantaneous

Figure 4.3 shows the time-averaged outboard and inboard pressure coefficient data plotted alongside the experimental values. The C_p data was taken at the same locations as the pressure ports on the physical model. The planes containing these ports are shown in figure 4.2. The URANS CFD data is in good agreement with the experimental data. The results for the inboard plane are also in good agreement, but it is clear that the flow control has less effect in this region.
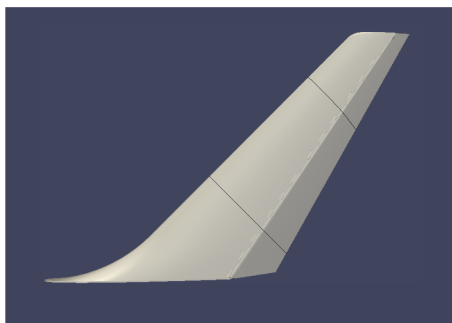
Figure 4.2: Pressure port planes
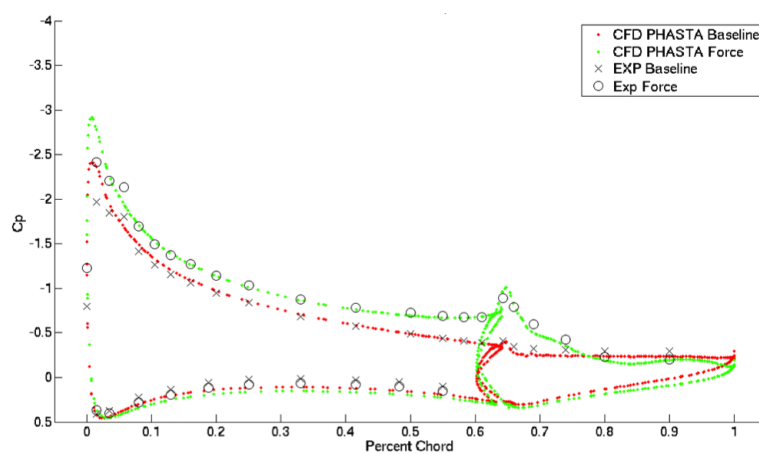
(a) Outboard
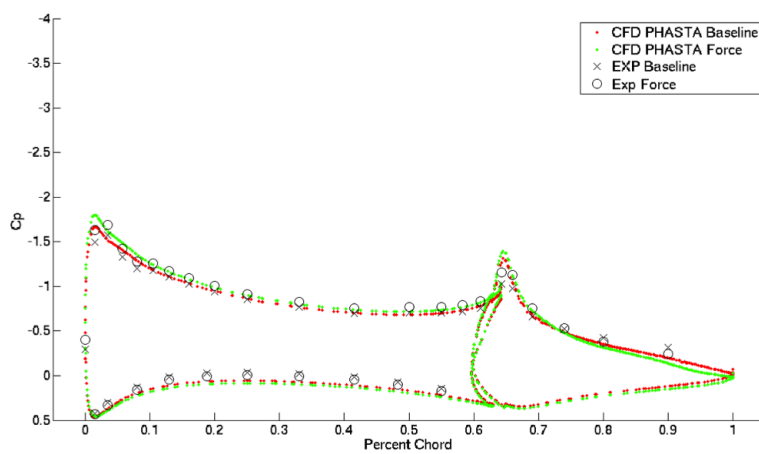
(b) Inboard

Figure 4.3: C_p - time average

Simulations were run to test the effect of a 180° phase offset between even and odd jets on time-averaged C_y and C_p. That is, the even jets are in the suction phase when the odd jets are blowing, and vice versa. It was found that there is virtually no difference between the two cases; the difference in time-averaged C_y is less than 1%. However, figure 4.4 shows there is a major difference in amplitude of the unsteady C_y.
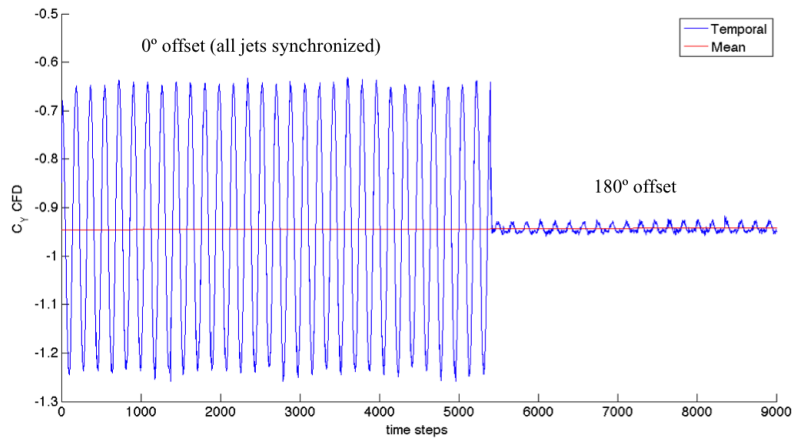
Figure 4.4: C_y - instantaneous

Figure 4.5 shows time-averaged C_p over the suction side of the vertical tail, for the baseline, jets in-phase, and jets out-of-phase cases.
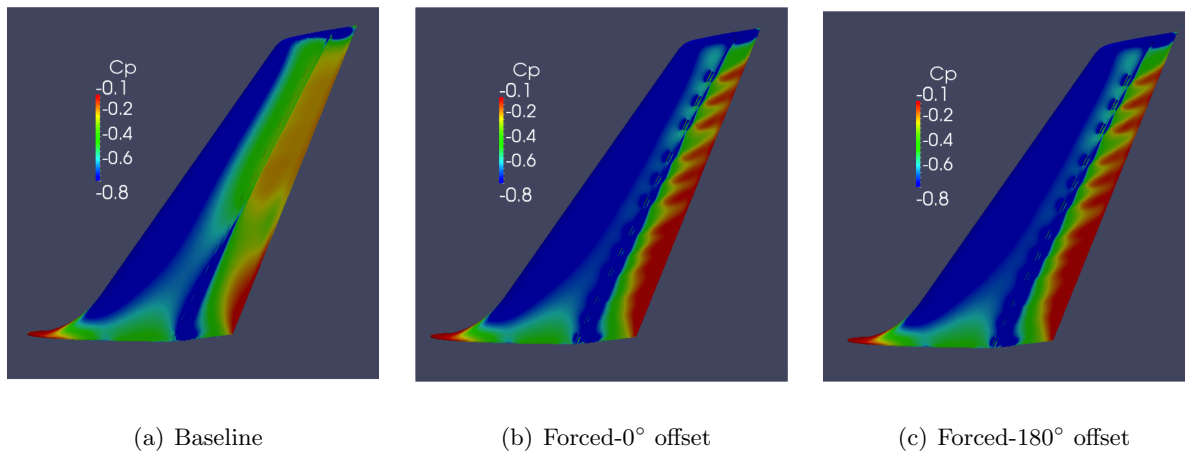
(a) Baseline   (b) Forced-0° offset   (c) Forced-180° offset

Figure 4.5: C_p - time average

Figures 4.5(b) and 4.5(c) are nearly identical, which is in agreement with 4.4. Figure 4.6 shows the time-averaged C_p on a cross-section through the outboard plane. This complements figure 4.3(a) in showing the change in C_p between the baseline and forced cases.


(a) Baseline

(b) Forced - 0° offset
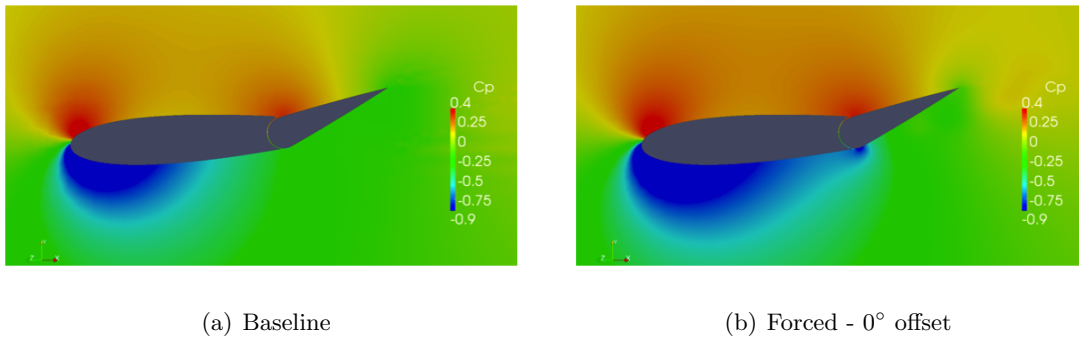
Figure 4.6: C_p - outboard plane

The difference in C_y amplitude for these two cases can be explained by comparing them at different phases of the jet cycle. Figure 4.7 shows C_p on the suction side for 4 phases of a simulation where the jets are synchronized. It is clear that the pressure shifts dramatically between the onset of blowing and the onset of suction. Figure 4.8 shows a different evolution of surface pressure when the jets are off-phase. These results are consistent with those shown in figure 4.4.

(a) 0°

(b) 90°
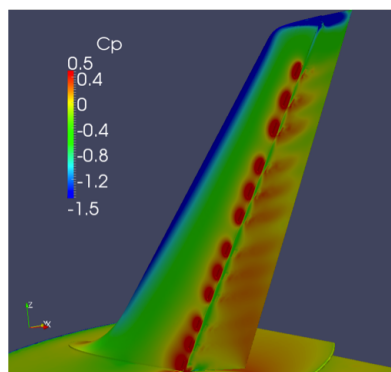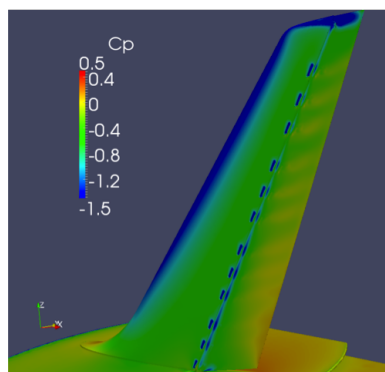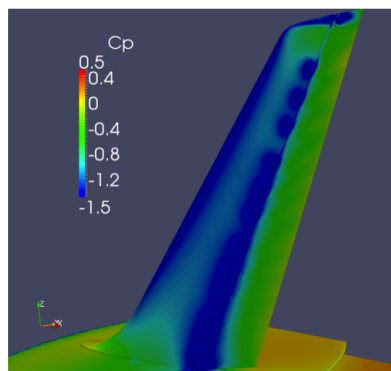
(c) 180°
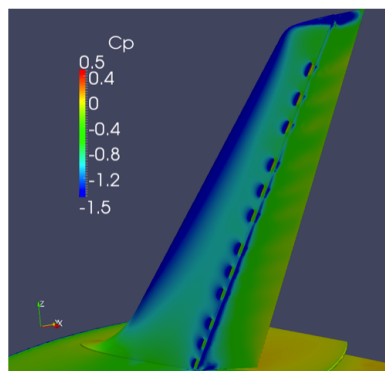
(d) 270°

Figure 4.7: C_p - 0° offset
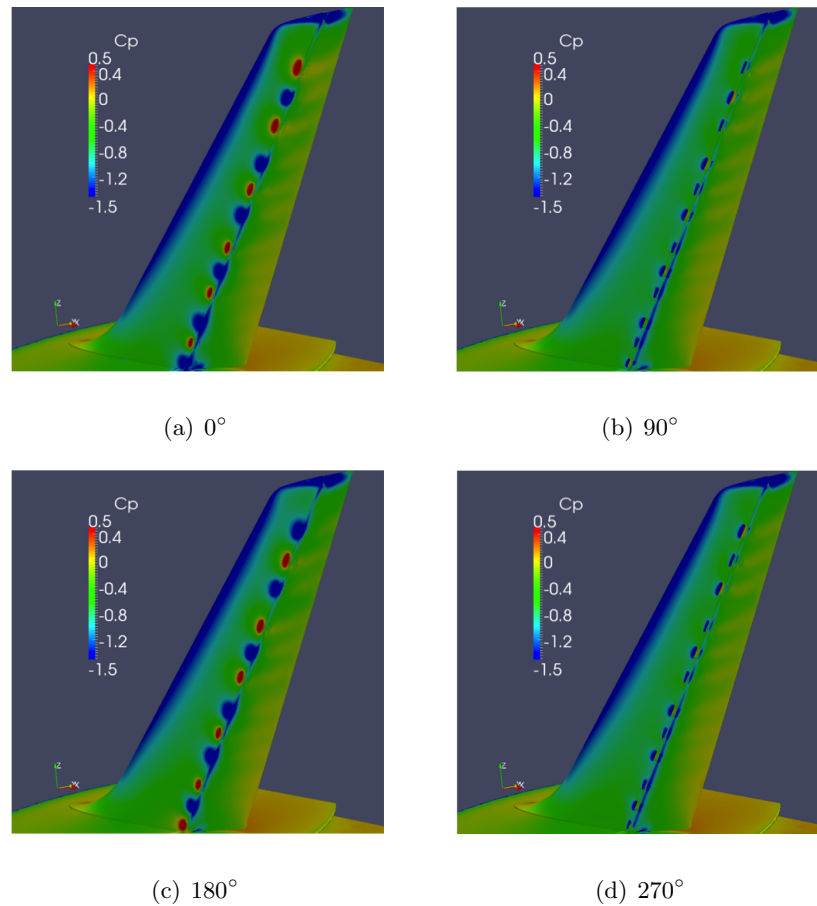
(a) 0°

(b) 90°

(c) 180°

(d) 270°

Figure 4.8: C_p - 180° offset

The effect of time step size on the solution was also investigated. When the same simulations were run with different time steps, the results show small differences up to a step size of 12 time steps per jet cycle. Step sizes of 180, 90, 45, 20, and 12 time steps per cycle were tested. The difference in time-averaged C_y with respect to 180 is very small ($< 1\%$) for all except 12, which is slightly higher. An examination of the instantaneous side force also reveals the gradual loss of accuracy with increasing time step. Figure 4.9(b) shows a marked increase in amplitude with increasing time step size, although it is not clear from this picture why the mean C_y for a step size of 12 time steps per jet cycle is different than the rest.
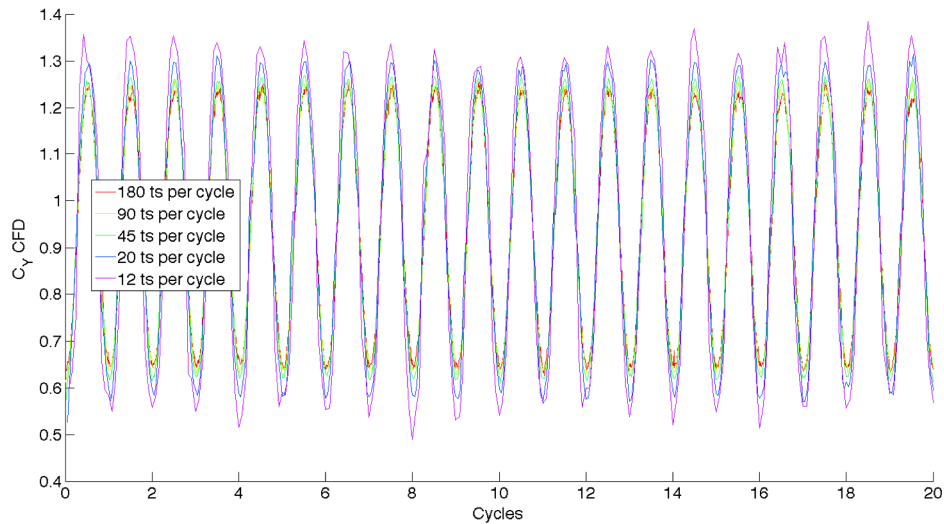
(a) C_y - instantaneous
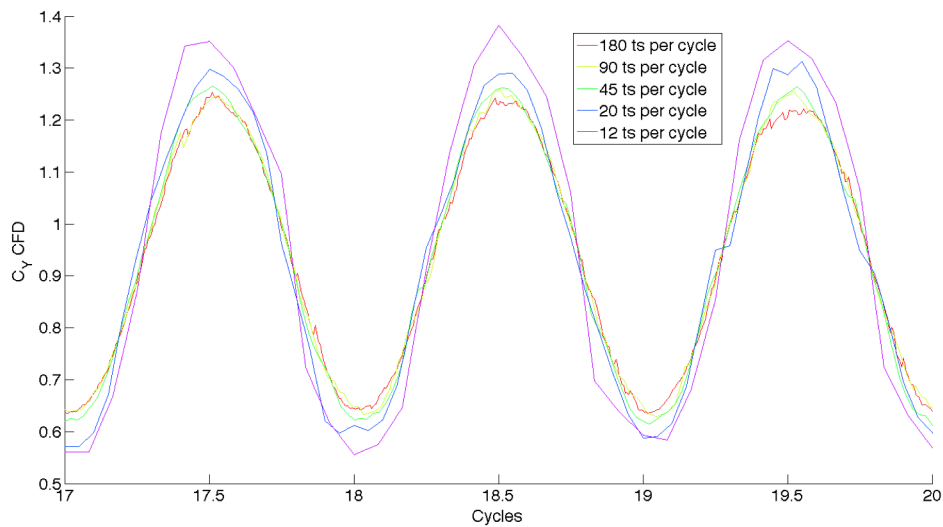
(b) C_y - instantaneous (3 periods)

Figure 4.9: C_y - instantaneous

The discrepancy is explained by figure 4.10, which shows the evolution of the mean C_y, where the mean was taken over 3 jet cycles. Increasing the time step beyond T/20 introduces a slow drift to the mean.
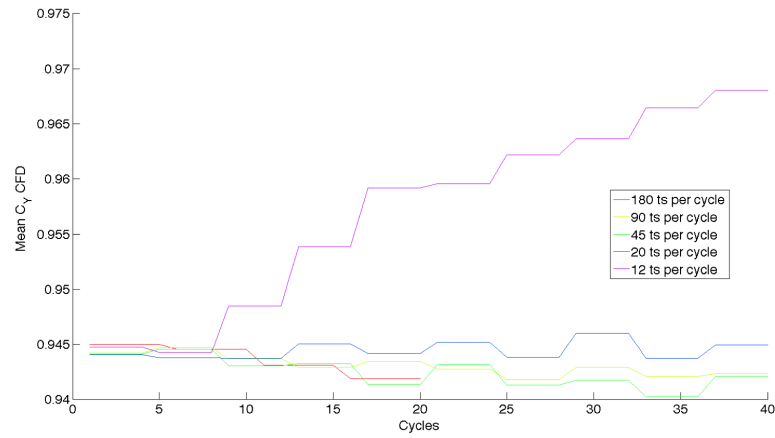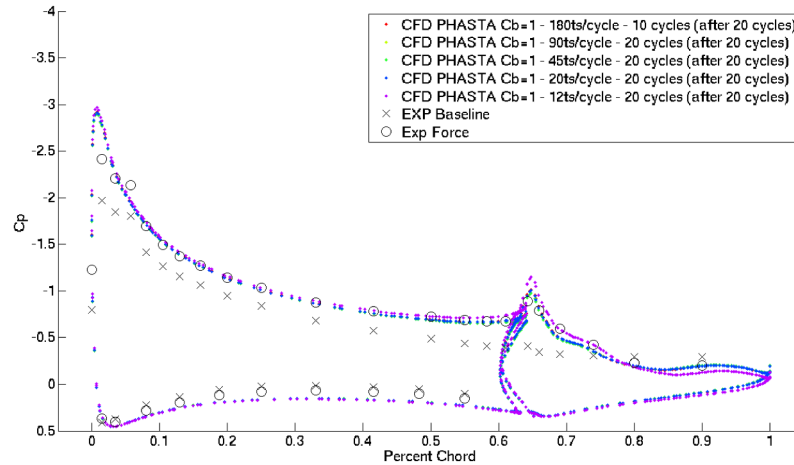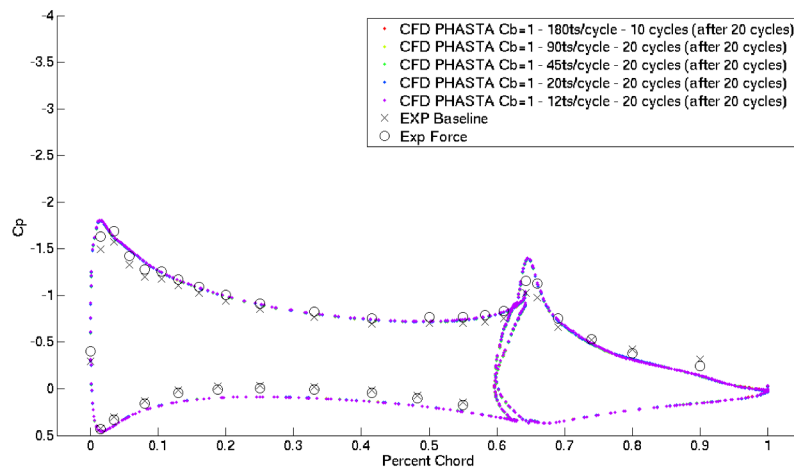
Figure 4.10: Evolution of mean C_y

Lastly, figure 4.11 shows that the outboard and inboard C_p is also predicted well by Phasta at larger time steps.

(a) Outboard

(b) Inboard

Figure 4.11: C_p - time average

4.2   Beta Model - $\beta=0°$, $\delta=30°$

This section will address the results obtained for the Beta model at a sideslip angle of $0°$ and a rudder deflection angle of $30°$. Steady blowing at 3 levels was used: V_{max}/π ($C_b = 1$), $V_{max}/2$, and $2\times V_{max}/\pi$. V_{max} for the cut jets was determined by equating the mass flux through its rectangular blowing face with the mass flux through the circular diaphragm of the full jet.

Figure 4.12 compares the time-varying C_y for the full and cut jet models with different combinations

of blowing: 0-1 means the odd jets are off while the evens are blowing, 1-1 means all jets are blowing, and 1-M1 means odd jets are blowing while the evens are in suction (jets are numbered from tip to root). The same RANS model was used, with a time step size of 0.00125 seconds. It should be noted that the baseline transient in the first 270 time steps was left out. The curves for both jets follow fairly closely for $V_{max}/2$ and $2\times V_{max}/\pi$, however, they are clearly very different for V_{max}/π. There is also not a large difference in side force coefficient between the baseline and V_{max}/π cases, which might suggest that steady blowing at this level is not enough to re-attach the flow. The mesh size in the refinement regions behind the rudder and downstream wake, in these cases, is rather conservative. It is most likely unable to resolve the separated shear layer for V_{max}/π.
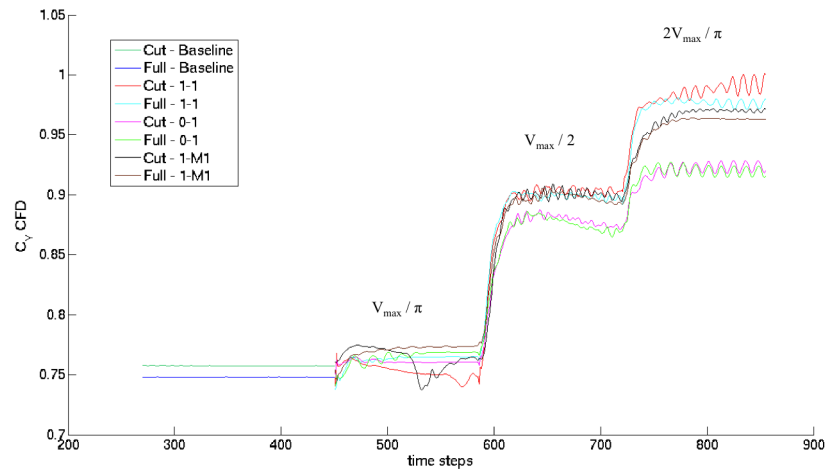

Figure 4.12: C_y

The baseline C_y for both cases is steady on a large time scale, where each is offset from the other by a small amount. But it is interesting to look at each one on a smaller scale, as shown in figure 4.13. It then becomes obvious that when the jets are off, they resonate due to the cross flow, and with different frequencies. This is expected however, because the cut jets have a shorter throat than the full jets, and therefore, should resonate with a higher frequency.
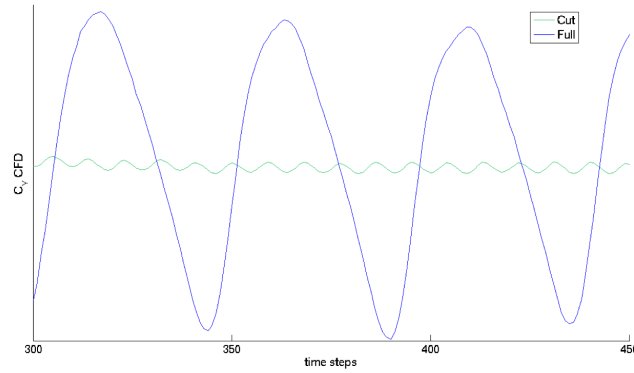
Figure 4.13: C_y - baseline

The effect of the jets can also be illustrated with velocity vectors. Figure 4.14 shows a slice through the middle of the 5th jet from the tip, for the baseline case. The time-averaged in-plane velocity vectors are shown, and the background is colored by the time-averaged out-of-plane speed. This massively separated flow is characterized by a backflow near the rudder surface, which is a part of a large wake behind the rudder. The same slice is shown in figure 4.15, but with all jets blowing at $2 \times V_{max}/\pi$. The added momentum essentially eliminates this velocity deficit, and keeps the flow attached the surface.
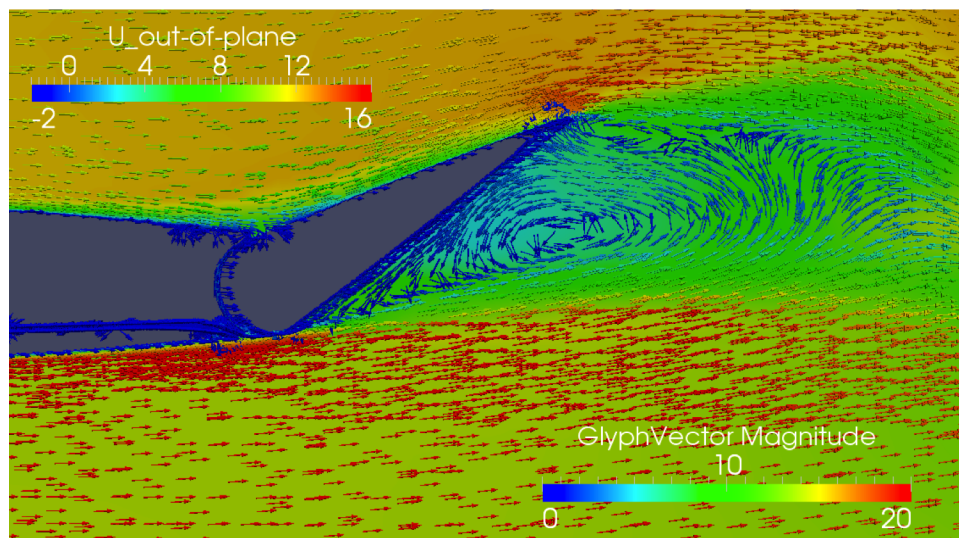

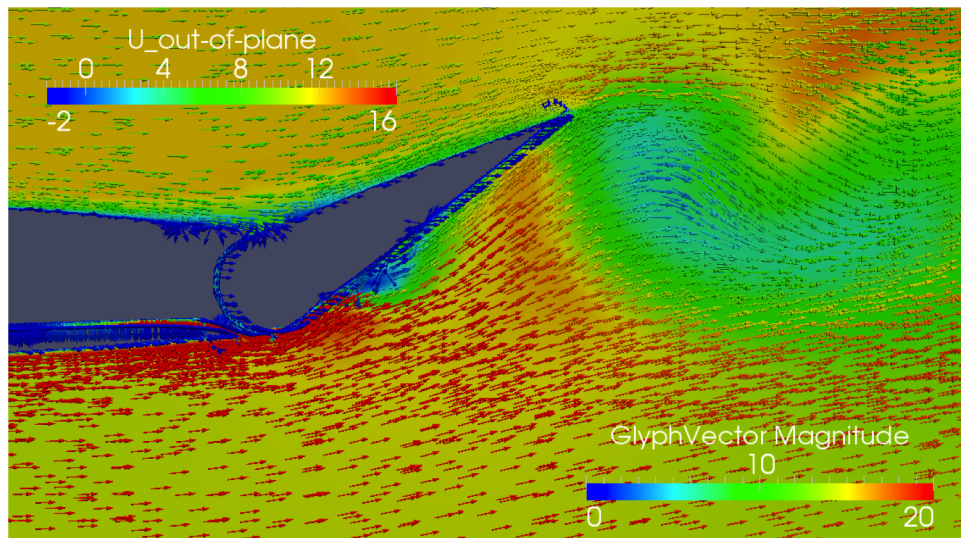Figure 4.14: In and out-of-plane velocity - Baseline

Figure 4.15: In and out-of-plane velocity - $2\times V_{max}/\pi$

Figures 4.16 - 4.18 show time-averaged normalized speed isosurfaces for the case where all 12 jets are blowing. The jets create a series of ridges and valleys of constant speed along the span, which strongly suggests that the jets are interacting and interfering with each other. These interactions are not desirable because they compromise the contribution of added momentum to the flow from each jet. The influence of the cross-flow forces the valleys to turn toward the freestream direction, where each valley is bounded by a ridge that eminates from the root side of the jets. The differences between the cut and full jet isosurfaces are fairly small, which is in agreement with figure 4.12. Comparing figures 4.17 and 4.18, the higher blowing makes the ridges in the middle and at the tip larger, while the ridges near the root are nearly unaffected. Comparing the baseline isosurfaces with the forced near the root, the jets are improving the velocity deficit very little, if any. This is because the flow is largely attached near the root for the baseline case. The reason for this is partly because the root vortex is helping to attach the flow to the rudder, with or without the jets activated. This result is consistent with the inboard C_p plot in figure 4.3(b), which also demonstrated little improvement. This vortex exists because of the gap between the rudder and fence.
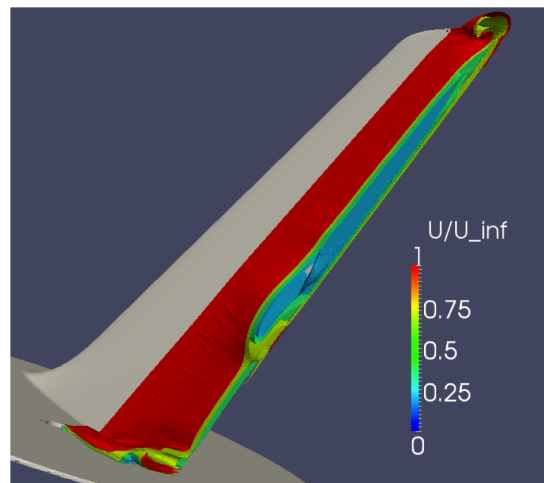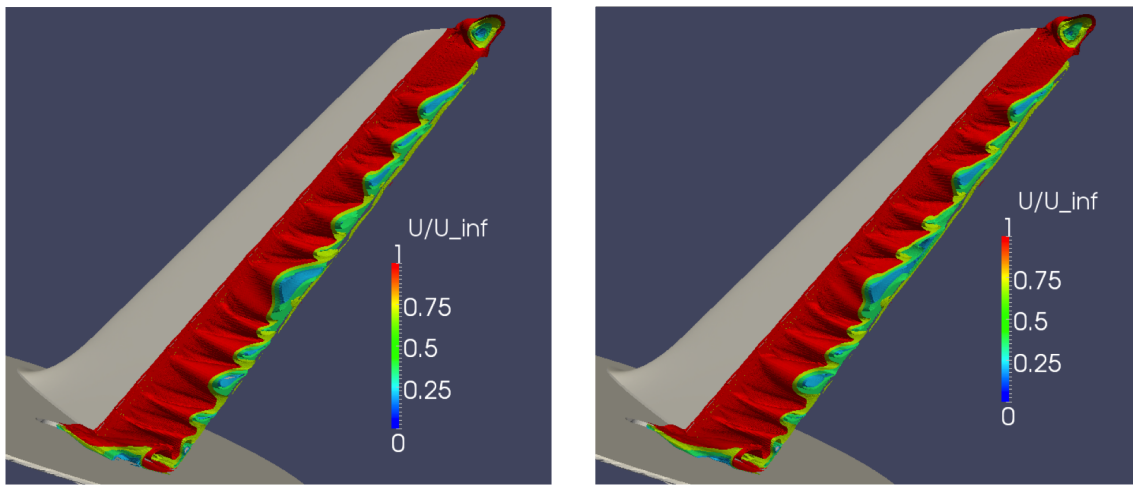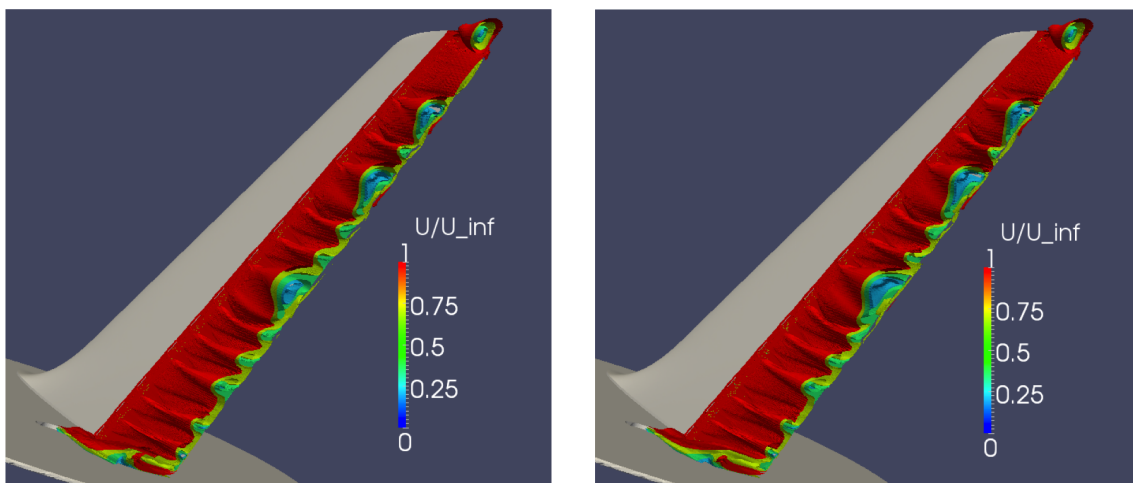
Figure 4.16: Normalized speed - baseline

(a) Cut jets

(b) Full jets

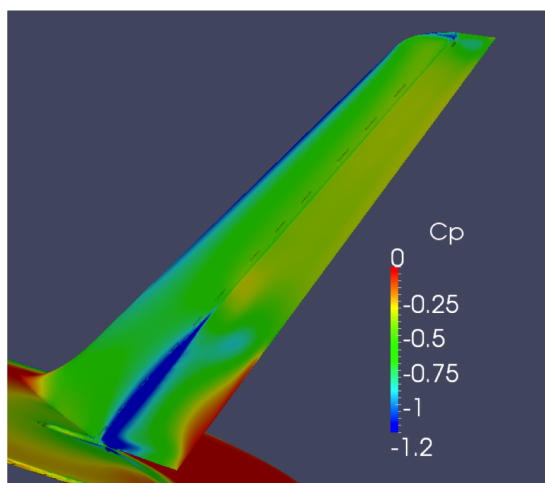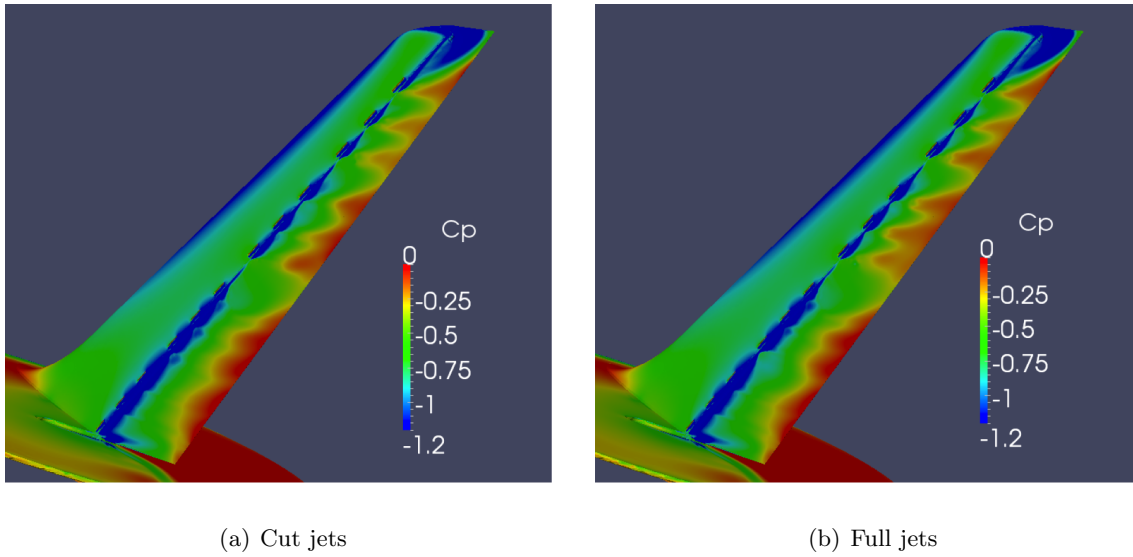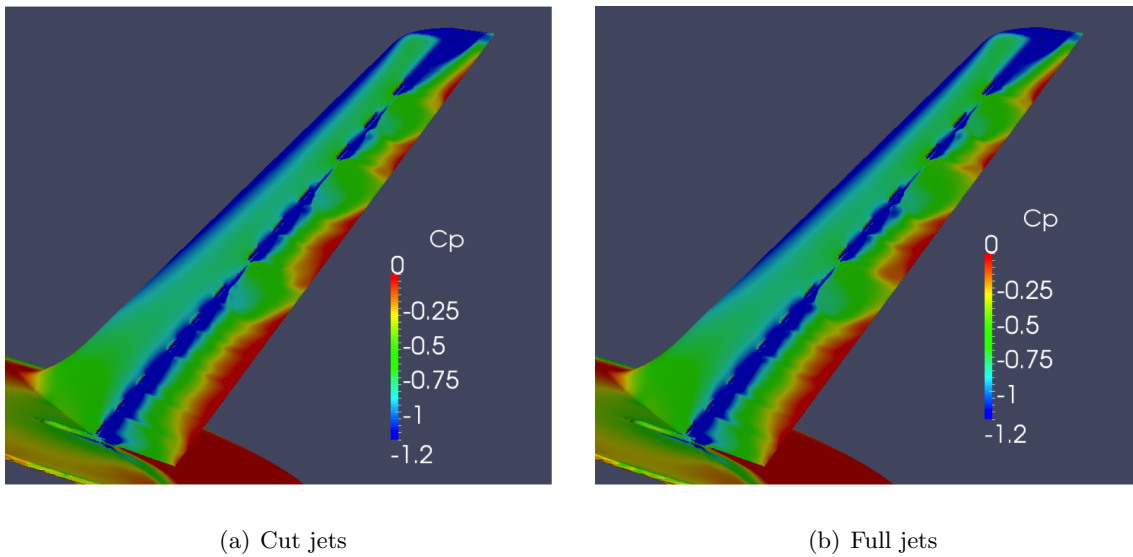Figure 4.17: Normalized speed - $V_{max}/2$

(a) Cut jets

(b) Full jets

Figure 4.18: Normalized speed - $2 \times V_{max}/\pi$

Figures 4.19 - 4.21 show time-averaged C_p for the same cases. The ridges and valleys are depicted by spanwise alternating patterns of red and green.

Figure 4.19: C_p - baseline

(a) Cut jets

(b) Full jets

Figure 4.20: C_p - $V_{max}/2$

(a) Cut jets

(b) Full jets

Figure 4.21: C_p - $2 \times V_{max}/\pi$

4.3   Beta-scaled Model - $\beta{=}0°$, $\delta{=}30°$

Finally, the URANS results for the Beta-scaled model will be discussed. The jets underwent steady blowing at two levels used previously: $V_{max}/2$ and $2 \times V_{max}/\pi$, and with a time step size of 0.00125 seconds. The mesh has similar characteristics as that used with the Beta model. C_y data for two cases is shown in figure 4.22: one where all jets are blowing (1-1) and one where the odd

jets are off and the evens are blowing (0-1). The 1-1 case produced a lower C_y for $V_{max}/2$, which is in contrast with the Beta model results. Figure 4.24 shows the time-averaged normalized speed isosurfaces for this same case. The ridges and valleys seen on the Beta model are also present on this model. The detachment of the isosurfaces in figure 4.25(a) is less severe than in figure 4.24(a), although it is not yet clear whether or not the higher blowing improves the jet interaction dynamics.
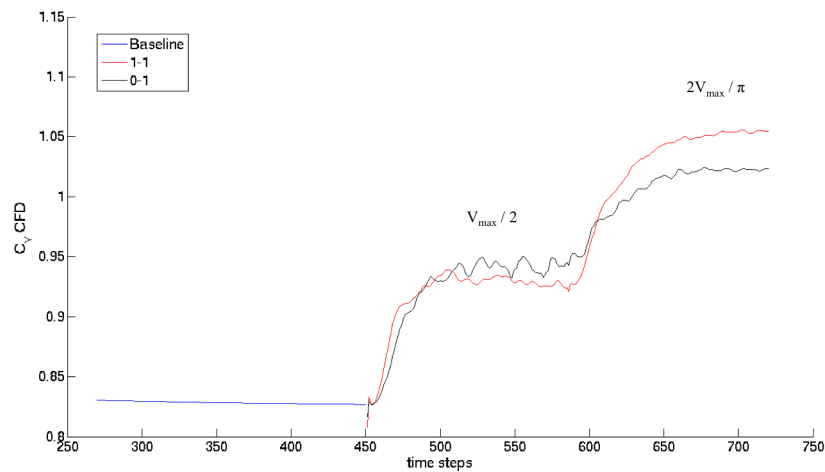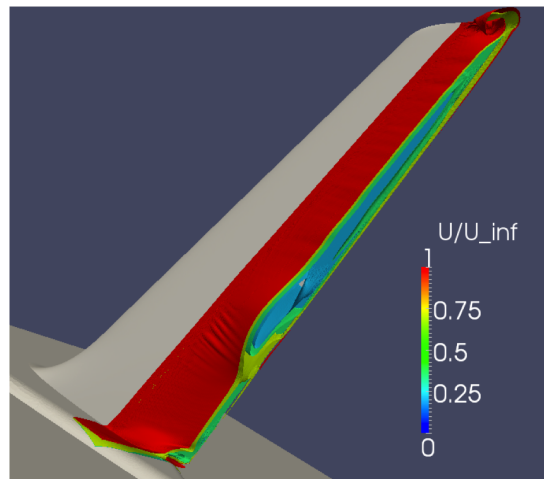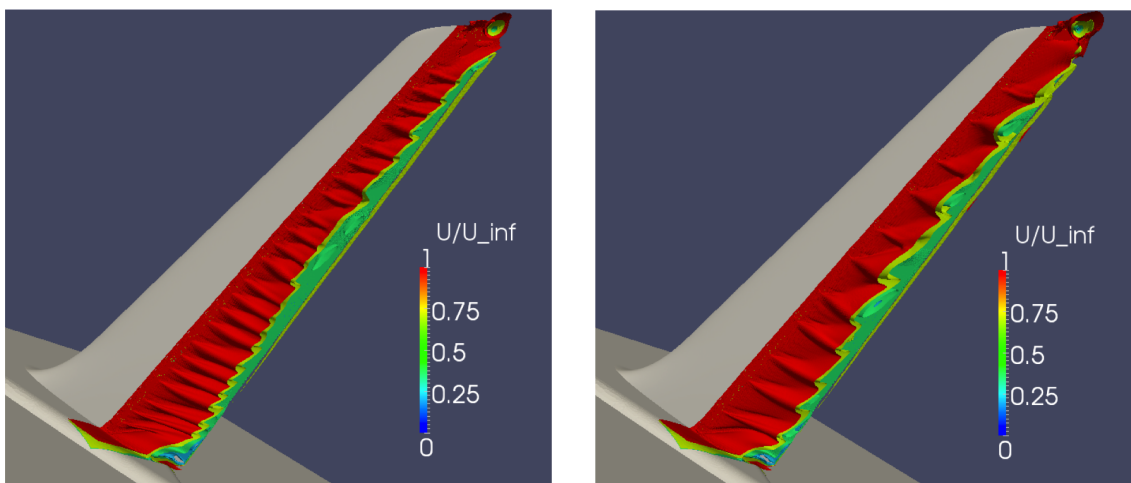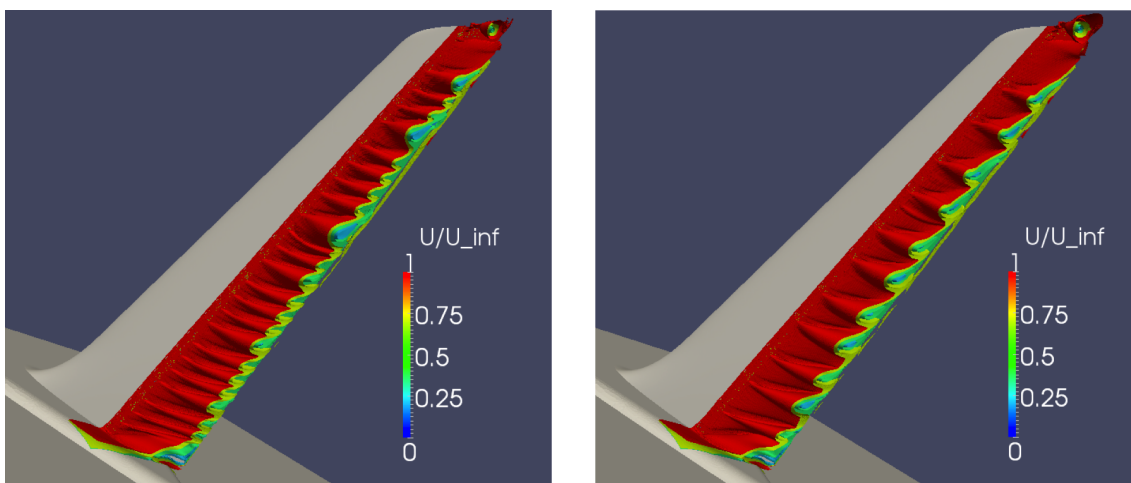

Figure 4.22: C_y

Figure 4.23: Normalized speed - baseline

(a) 1-1

(b) 0-1

Figure 4.24: Normalized speed - $V_{max}/2$

(a) 1-1

(b) 0-1

Figure 4.25: Normalized speed - $2 \times V_{max}/\pi$

Chapter 5

Conclusions and Future Work

Two vertical tail models were considered in this study, the Beta and Beta-scaled models. Phasta was used to run URANS simulations on the Beta model with a Reynolds number of 3.6×10^5, sideslip angle of $5°$, and rudder deflection angle of $20°$. When a C_b of 1.0 and a time step size of 180 time steps per jet cycle were used with the jets in locked phase, an approximate 14% increase in C_y magnitude was seen with respect to the baseline. The C_p measured in the plane containing the outboard pressure ports increased in magnitude, however, it did not change appreciably at the inboard pressure ports. The C_p data was in good agreement with experimental values. Additionally, it was found that introducing a $180°$ offset between even and odd jets produced the same C_y and C_p as the $0°$ case. The time step study done on this model showed that C_y stays fairly constant for step sizes of 180, 90, 45, and 20 time steps per jet cycle, but changes significantly with 12 time steps per cycle. The inboard and inboard C_p were predicted well by Phasta, even at 12 time steps per cycle.

URANS data was also gathered from the Beta model for a sideslip angle of $0°$ and rudder deflection angle of $30°$. These simulations used steady blowing, with a time step size of 0.00125 seconds. It was found that turning all 12 jets on and setting the maximum velocity on the diaphragm to $2 \times V_{max}/\pi$ resulted in the biggest change in C_y with respect to the baseline. Both the full and cut jets showed a similar time evolution of C_y for blowing levels of $V_{max}/2$ and $2 \times V_{max}/\pi$. The normalized speed isosurfaces form ridges and valleys along the span, suggesting that the jets are interfering with each other.

The Beta-scaled model simulations were run at a Reynolds number of 7.1×10^5, sideslip angle of $0°$ and rudder deflection angle of $30°$. Steady blowing with the cut jets and a time step size of 0.00125 seconds were used. An interesting result from these runs was that when a blowing level of $V_{max}/2$ was used, the instantaneous C_y seen when only the even jets were on was higher than when all the jets were on. Similar to the Beta model speed isosurfaces, these also formed ridges and valleys along the span.

These simulations will pave the way for future simulations that will shed light on the most important questions. In particular, the means by which the jets influence each other needs to be addressed. Analyses of vorticity, in addition to velocity, may be of some use here. It is possible that different spanwise jet spacing configurations should be tested, because maybe this is the key to more efficient use of the jets. Changing the jet orientation could also help in this area, for example, by making them parallel to the freestream. It is also necessary to cover a wide parameter space, in order to understand better how the synthetic jets behave for different sideslip and rudder deflection angles. It is equally important to conduct refinement studies to determine an adequate initial mesh. As the model is scaled up further, fluctuation-based adaption will become increasingly important due to constraints on the memory available for creating an initial mesh.

References

[1] M. Amitay, D. R. Smith, V. Kibens, D. E. Parekh, and A. Glezer. Aerodynamic flow control over an unconventional airfoil using synthetic jet actuators. *AIAA*, 39(3):361–370, 2001.

[2] L. P. Franca and S. Frey. Stabilized finite element methods: II. The incompressible Navier-Stokes equations. *Computer Methods in Applied Mechanics and Engineering*, 99:209–233, 1992.

[3] A. Glezer and M. Amitay. Synthetic Jets. *Annu. Rev. fluid Mech.*, 34:503–29, 2002.

[4] P. M. Gresho. Some current CFD issues relevant to the incompressible Navier-Stokes equations. *Computer Methods in Applied Mechanics and Engineering*, 87:201–252, 1991.

[5] T. J. R. Hughes. *The Finite Element Method: Linear Static and Dynamic Finite Element Analysis*. Prentice Hall, Englewood Cliffs, NJ, 1987.

[6] K. E. Jansen, C. H. Whiting, and G. M. Hulbert. A generalized-α method for integrating the filtered navier-stokes equations with a stabilized finite element method. *Computer Methods in Applied Mechanics and Engineering*, 190:305–319, 2000.

[7] F. Shakib. http://www.acusim.com, 2000.

[8] P. R. Spalart and S. R. Allmaras. A one-equation turbulence model for aerodynamic flows. *AIAA*, 1992.

[9] C. A. Taylor, T. J. R. Hughes, and C. K. Zarins. Finite element modeling of blood flow in arteries. *Computer Methods in Applied Mechanics and Engineering*, 158:155–196, 1998.

[10] C. H. Whiting and K. E. Jansen. A stabilized finite element method for the incompressible navier-stokes equations using a hierarchical basis. *International Journal of Numerical Methods in Fluids*, 35:93–116, 2001.